

Microscopic factors modulating the interactions between the SARS-CoV-2 main protease and α -ketoamide inhibitors

Luigi Genovese,[†] William Dawson,[‡] Takahito Nakajima,[‡] Viviana Cristiglio,[¶]
Valérie Vallet,[§] and Michel Masella^{*,||}

[†]*Univ. Grenoble Alpes, CEA, IRIG-MEM-L-Sim, 38000 Grenoble, France*

[‡]*RIKEN Center for Computational Science, Kobe, Japan*

[¶]*Institut Laue Langevin, 71 Av. des Martyrs, 38000 Grenoble France*

[§]*Université de Lille, CNRS, UMR 8523 - PhLAM - Physique des Lasers Atomes et
Molécules, F-59000 Lille, France*

^{||}*Laboratoire de Biologie Structurale et Radiobiologie, Service de Bioénergétique, Biologie
Structurale et Mécanismes, Institut Joliot, CEA Saclay, F-91191 Gif sur Yvette Cedex,
France*

E-mail: michel.masella@cea.fr

Abstract

1
2 We performed 10 ns scale molecular dynamics simulations of 6 SARS-CoV-2 main
3 protease/ α -ketoamide inhibitor complexes in aqueous solution, in the phase before the
4 inhibitor covalently binds to the protease's catalytic cysteine, using a polarizable multi-
5 scale molecular modeling approach. For each simulation, 100 \mathbf{M}^{Pro} /inhibitor snapshots
6 (about 4 800 atoms) were extracted along the last 2 ns simulation segments. They
7 were post processed using a fully quantum mechanical $O(N)$ approach to decompose
8 the protease into sets of fragments from which we computed the mean local interaction
9 energies between the inhibitors and the different pockets of the protease catalytic do-
10 main. Contrary to earlier results, our analysis shows that the protease pocket S2 to be
11 a key anchoring site able to lock within the catalytic domain an α -ketoamide inhibitor
12 even before covalent bonding to the protease catalytic cysteine occurs. To target that
13 pocket our computations suggest to consider hydrophobic groups, like cyclo-propyl or
14 cyclo-hexyl.

15 Several new drugs targeting the SARS-CoV-2 main viral protease \mathbf{M}^{pro} (also called
16 $\mathbf{3CL}^{\text{pro}}$) have been shown to be promising (or promising lead) compounds to develop new
17 antiviral treatments for COVID-19.¹⁻⁵ All of these inhibitors have been built from standard
18 docking approaches by inferring the microscopic factors modulating the strength of their in-
19 teraction with \mathbf{M}^{pro} from experimental structural data and then selected from experimental
20 trial-and-error approaches. To speed up the optimization process or the development of new
21 \mathbf{M}^{pro} inhibitors, an information of pivotal importance is the knowledge of reliable data that
22 accurately quantify the strength of the microscopic interactions at the origin of the stability
23 of \mathbf{M}^{pro} /inhibitor complexes.

24 Despite being heavily computationally demanding, Quantum chemical Methods, QM,
25 are the most reliable theoretical approaches to investigate microscopic systems. Recently
26 one of us proposed an efficient quantum $O(N)$ method based on Daubechies wavelets^{6,7}
27 allowing one to investigate molecular systems comprising thousands of atoms on modern
28 supercomputing systems. An interesting feature of that approach is its ability to decompose
29 a molecular system into fragments from which one may compute a map summarizing the
30 microscopic local interactions occurring within a molecular complex.^{8,9} In the present study,
31 we combine such a QM approach with a simulation stage based on a multi-scale polarizable
32 Molecular Modeling, MM, one^{10,11} to investigate the Potential Energy Surface, PES, of
33 \mathbf{M}^{pro} /inhibitor complexes from Molecular Dynamics, MD, simulations in the aqueous phase.
34 A set of complex structures are extracted from the MD trajectories and post processed using
35 the QM approach both to assess the reliability of the MM approach and to compute mean
36 \mathbf{M}^{pro} /inhibitor complex local interaction maps that account for structural fluctuations.

37 Recently, theoretical studies have appeared investigating the stability of \mathbf{M}^{pro} complexes
38 with marketed drugs^{12,13} (from chloroquine to curcumin and including the new peptide-like
39 inhibitor "N3"²), with marine natural product putative inhibitors¹⁴ or with hydroxyethy-
40 lamine analogs¹⁵ using standard pairwise force field-based MD approaches or the QM-based
41 Fragment Molecular Orbital scheme (applied to the \mathbf{M}^{pro} /N3 complex X-ray crystallographic

42 structure¹⁶). Instead we employ here our sequential MM – QM (not to be confused with tra-
43 ditional QM/MM methods) scheme to investigate the interaction of **M^{pro}** with four strong
44 peptidomimetic α -ketoamide inhibitors recently synthesized by the Hilgenfeld’s team¹ (*i.e.*
45 inhibitors **13a**, **13b**, **14b** and **11r**) as well as two such inhibitors characterized by a weak
46 or no inhibitory potency for the main proteases of a large set of coronaviruses¹⁷ (inhibitors
47 **11p** and **11f**, see Figure 1). Note that the lack of inhibitory potency does not prejudice
48 of the ability of an ”inhibitor” to interact with the **M^{pro}** catalytic site or to form a stable
49 complex.¹⁷ In addition to being unlikely toxic, α -ketoamide inhibitors are able to form a
50 covalent bond with the **M^{pro}** catalytic cysteine residue (based on a reversible mechanism¹⁸)
51 that stabilizes **M^{pro}**/inhibitor complexes. However we focus our study to complexes corre-
52 sponding to the pre-reactive state before the formation of a covalent bond between **M^{pro}** and
53 the inhibitors, a state that is also pivotal to understanding the stability of **M^{pro}**/inhibitor
54 complexes.^{19,20} Together with earlier theoretical studies, our present data will allow us to
55 promote a more global understanding of the microscopic factors modulating the interaction
56 of **M^{pro}** with putative inhibitors.

57 **M^{pro}**/inhibitor complex starting structures are built from the X-ray PDB structure
58 6Y7M²¹ corresponding to the Hilgenfeld’s inhibitor **13a**¹ by manually docking the other in-
59 hibitors to best fit the **13a** conformation. The **M^{pro}** catalytic pair His⁴¹/Cys¹⁴⁵ is considered
60 in its ionic form (its standard protonation state in **M^{pro}** as shown by a joint neutron/X-ray
61 study²² - see Supplementary Information): their side chains are an imidazolium and a thiolate
62 group, respectively. The inhibitors are not covalently bonded to Cys¹⁴⁵. For each complex,
63 we performed 10 independent NPT MD simulations (corresponding to different starting ve-
64 locity sets) in the aqueous phase at the 10 ns scale using the code POLARIS(MD).²³ Protease
65 dimerization is needed for catalytic activity as local dimer interactions stabilizes the catalytic
66 pocket shape.²⁴ We consider here a single **M^{pro}** monomer and we account for the presence
67 of a second unit by harmonically restraining the positions of the **M^{pro}** backbone carbons C $_{\alpha}$
68 that are more than 5 Å from any inhibitor atom.

69 \mathbf{M}^{pro} /inhibitors complexes are modeled using an updated version of the polarizable all
70 atoms force field TCPEp.²⁵ Besides standard additive potentials like Coulombic and disper-
71 sion energy terms, TCPEp also includes a many-body polarization term (based on an induced
72 dipole moment approach including short-range damping effects) and many-body anisotropic
73 terms to model hydrogen bond networks. The TCPEp parameters are assigned to reproduce
74 high-level quantum *ab initio* computations regarding a training set of molecular clusters (see
75 Ref. 26 for instance). Water is simulated using an updated version of the coarse-grained
76 Polarizable Pseudo Particle, PPP, approach^{10,11} that improves ion hydration modeling. Pro-
77 tease/inhibitor complexes are embedded in rectangular boxes comprising about 57 000 PPP
78 particles. The force field and the accuracy of the coupled TCPEp/PPP approach to model
79 hydrated proteins and α -ketoamide inhibitors are discussed in the Supporting Information.

80 We also computed local \mathbf{M}^{pro} /inhibitors Potentials of Mean Force, PMFs, in aqueous
81 phase corresponding to the distance r between (1) the carbon atom connecting the ketoamide
82 moiety to the inhibitor main chain and (2) the \mathbf{M}^{pro} His¹⁶⁴ backbone carbon C using standard
83 Umbrella Sampling techniques coupled to our MD protocol. The r distance was scanned from
84 4 to 8 Å: within that distance domain we assume our MD protocol to provide a sampling of
85 the local \mathbf{M}^{pro} /inhibitor PES that is sufficiently accurate.

86 Along the last 2 ns MD segments, we extracted 100 \mathbf{M}^{pro} /inhibitor regularly spaced
87 snapshots (each comprising about 4 800 atoms) that were further investigated using a full QM
88 $O(N)$ approach based on Density Functional Theory with the Perdew-Burke-Erzerhof (PBE)
89 functional implemented by a Daubechies wavelets formalism.^{6,7} On modern supercomputing
90 systems the computation of a \mathbf{M}^{pro} /inhibitor complex PBE single energy point is achieved
91 within less than 2 hours using 1 024 computational cores. Note that the PBE energies
92 discussed below (unless otherwise stated) have been corrected by including D3 dispersion
93 terms.²⁷ The localized basis functions used in that QM scheme allow one to readily gather
94 system atoms into “fragments”(f) and to approximate the system density matrix F as a sum
95 of fragment density matrices F^f up to a desired level of accuracy measured by the ”fragment

96 purity” index $\Pi^f = \mathbf{Tr}((F^f)^2 - F^f)$.^{8,9} A fragmentation is physically meaningful when all
 97 the $|\Pi^f|$ s are small, typically about 5 % as shown by an earlier study⁹ and as set here. Such
 98 a fragmentation can be defined common to all the snapshots of an entire MD trajectory.
 99 A quantum \mathbf{M}^{pro} /inhibitor interaction map may be thus readily drawn from the quantum
 100 energies $\delta\bar{U}^{fi}$ measuring the magnitude of the interactions between the \mathbf{M}^{pro} fragments and
 101 the inhibitor (taken as a single fragment i) averaged over our MD simulations to account
 102 for \mathbf{M}^{pro} /inhibitor complex structural fluctuations. Note that, the $\delta\bar{U}^{fi}$ s computed in the
 103 present study do not include the D3 dispersion correction, they measure the strength of the
 104 local \mathbf{M}^{pro} /inhibitor repulsion-exchange and electrostatic interactions. They have thus to be
 105 considered to compare \mathbf{M}^{pro} /inhibitor interaction patterns among them and not to discuss
 106 the global strength of \mathbf{M}^{pro} fragment/inhibitor interactions.

107 Along all independent MD simulations, inhibitors **11r**, **13a**, **13b** and **14b** interact
 108 strongly with the \mathbf{M}^{pro} catalytic pair His⁴¹/Cys¹⁴⁵, see Figure 1. The His⁴¹ imidazolium
 109 is hydrogen bonded to one of the ketoamide oxygens and the Cys¹⁴⁵ sulfur strongly interacts
 110 with both the ketoamide sp² carbons (the corresponding mean distances are about 2.8 Å).
 111 The mean \mathbf{M}^{pro} /inhibitor distance r defined above is about 5.3 Å and these inhibitors are
 112 also hydrogen bonded to residues His¹⁶³, His¹⁶⁵, Glu¹⁶⁶ and Asn¹⁸⁹ backbones or side chains
 113 along all simulations in agreement with experiments.¹ However large structural fluctuations
 114 of the inhibitor side chains can be observed, in particular the Boc group within the \mathbf{M}^{pro} S4
 115 pocket.

116 The above “standard” \mathbf{M}^{pro} /inhibitor interaction pattern is also observed along 6 \mathbf{M}^{pro} /**11p**
 117 simulations (we recall that **11f** and **11p** are non-inhibitory substrates). Along them the mean
 118 dihedral angle $\bar{\psi}^{\mathbf{11p}} = \langle \text{N} - \text{C} - \text{C} - \text{C} \rangle$ corresponding to atoms connecting the acetonitril
 119 moiety to the inhibitor main chain is about 180°. That moiety does not reside within pocket
 120 S2 and it is not hydrogen bonded to any \mathbf{M}^{pro} residue. Along 3 other simulations, this
 121 interaction pattern is strongly altered: $\bar{\psi}^{\mathbf{11p}} \approx -60^\circ$, $r \approx 7.2$ Å and the acetonitril moiety
 122 establishes hydrogen bonds with the Tyr⁵⁴ hydroxyl group and/or with the Gln¹⁸⁹ backbone.

123 Inhibitor **11f** maintains a “standard” interaction pattern only along 3 simulations: the **11f**
124 Boc group resides then at the ‘entrance’ of pocket S2 (it is not as deeply buried in that
125 pocket as the cyclo-hexyl and cyclo-propyl groups of inhibitors **13a** and **13b**, see Support-
126 ing Information), in agreement with experiments regarding the SARS-CoV main protease.¹⁷
127 Along all the other **11p/11f** simulations, the inhibitor leaves the catalytic site.

128 The propensity of inhibitors to maintain a standard interaction pattern may be assessed
129 from our PMF(r) profiles, see Figure 2. The four strong inhibitors PMFs are close: they
130 present a single minimum at $r \approx 5.3$ Å and they increase then by up to 5 kcal mol⁻¹ at
131 $r \approx 7.5$ Å. The PMF of **11f** also presents a minimum at $r \approx 5.0$ Å but it increases until it
132 reaches a weak energy barrier of 2 kcal mol⁻¹ at $r \approx 6.0$ Å explaining the propensity of **11f**
133 to escape from the catalytic site along our simulations. We computed three PMF profiles
134 for **11p** corresponding to the ψ^{11p} dihedral angle restrained harmonically to a value of 60
135 (PMF₆₀^{11p}), -60 (PMF₋₆₀^{11p}) and 180° (PMF₁₈₀^{11p}), respectively. These dihedral angle values
136 correspond to minimum locations on the acetronitryl dihedral energy profile discussed in
137 the Supporting Information. PMF₁₈₀^{11p} is close to the **11f** one with, however, with an even
138 weaker energy barrier (about 1 kcal mol⁻¹) at about 6.0 Å, whereas the lowest minima of
139 PMF₆₀^{11p} and PMF₋₆₀^{11p} are located at 6.8-7.0 Å. While we have not exhaustively sampled
140 the M^{pro}/inhibitor PESs,²⁸ the computed PMFs support the inhibitor behaviors along our
141 independent MD simulations.

142 We computed the MM and QM/PBE+D3 M^{pro}/inhibitor mean interaction energies $\Delta\bar{U}$
143 from 100 M^{pro}/inhibitor complex snapshots extracted along a single MD simulation for each
144 strong inhibitor **11r**, **13a**, **13b** and **14b**, and along three and five simulations corresponding
145 to different M^{pro}/inhibitors interaction patterns for **11p** and **11f**, respectively. $\Delta\bar{U}$ s are
146 computed as the difference between the M^{pro}/inhibitor complex energy and the energies of
147 M^{pro} and of the inhibitor alone in their complex geometry. Both these sets of $\Delta\bar{U}$ values are
148 linearly correlated. However the MM energies are more stable than the QM ones by about
149 20 %, see Figure 2. We have identified (see Supporting Information) that this discrepancy

150 does not arise from differences in MM and PBE+D3 descriptions of \mathbf{M}^{pro} /inhibitor short-
 151 range interactions, but rather from a PBE under-polarization of the \mathbf{M}^{pro} chemical bonds
 152 yielding a PBE electrostatic potential within the \mathbf{M}^{pro} catalytic pocket weaker by 20 %
 153 as compared to MM. A similar PBE bond under-polarization compared to a polarizable
 154 force field approach was already observed for liquid water.²⁹ Lastly, D3 and MM dispersions
 155 represent from 40 to 80 % of the absolute $\Delta\bar{U}$ values.

156 MM and PBE+D3 $\Delta\bar{U}$ values of the four strong inhibitors differ at most by 10% but they
 157 are all smaller than the **11p** value corresponding to a simulation along which that inhibitor
 158 maintain a standard interaction pattern. The inhibitor potency is thus not dominated by
 159 the sole strength of the \mathbf{M}^{pro} /inhibitor interaction but it results from complex interaction
 160 competitions between the inhibitor, the \mathbf{M}^{pro} enzyme and their chemical environment, as
 161 discussed in Ref. 1 and as suggested by our PMFs. Along the simulations where inhibitors
 162 **11p** and **11f** left the \mathbf{M}^{pro} catalytic site, MM and PBE+D3 $\Delta\bar{U}$ values are twice to three
 163 times weaker compared to simulations where the inhibitors maintain a standard interaction
 164 pattern with \mathbf{M}^{pro} .

165 Focusing now on the snapshot sets corresponding to a standard \mathbf{M}^{pro} /inhibitor inter-
 166 action pattern, *i.e.* the four strong inhibitors sets and those corresponding to simulations
 167 labeled 8 and 9 in Figure 2 for inhibitors **11f** and **11p**, respectively, our QM fragmentation
 168 yields temporally stable and almost identical \mathbf{M}^{pro} fragment patterns. Among the about 200
 169 fragments identified, about 20 of them (located at the inhibitor vicinity) interact noticeably
 170 with the inhibitor. Most of these fragments correspond to a single residue at the remarkable
 171 exception of the fragment Gly¹⁴³-Ser¹⁴⁴-Cys¹⁴⁵ that gathers the oxyanion residues and the
 172 catalytic cysteine. We assigned the fragments to the \mathbf{M}^{pro} catalytic domain pockets from dis-
 173 tance arguments, see Figure 3 where we also plot the mean energies $\Delta\bar{U}_{\text{inhi}}^{\text{pocket}}$ corresponding
 174 to the sum of the $\delta\bar{U}^{fi}$ energies running on the fragments belonging to a given pocket. For the
 175 four strong inhibitors and inhibitor **11f**, their $\Delta\bar{U}_{\text{inhi}}^{\text{pocket}}$ profiles are close: they interact the
 176 strongest with pocket S1'(which comprises the \mathbf{M}^{pro} catalytic pair) and in a negligible way

177 with pockets S3 and S4. The $\Delta\bar{U}_{\text{inhi}}^{\text{pocket}}$ profile of inhibitor **11p** differs noticeably compared
178 to the latter ones: **11p** interacts the strongest with pocket S2 and noticeably with pocket
179 S3. The dihedral angle $\bar{\psi}^{\text{11p}}$ is about 180° along the **11p** simulation 9: the **11p** acetonitril
180 moiety is outside of pocket S2 and the inhibitor phenyl group initially residing within the
181 pocket S4 core evolves to interact with the backbone CO groups of Val¹⁸⁶, Arg¹⁸⁸ and Thr¹⁹⁰
182 at the pockets S4/S2 boundary (see Supporting Information). The strongest interaction of
183 **11p** with pocket S2 may thus be considered as an artifact but this does not lead to change
184 the above conclusion about the difference in the $\Delta\bar{U}_{\text{inhi}}^{\text{pocket}}$ profiles. The energies $\Delta\bar{U}_{\text{inhi}}^{\text{pocket}}$
185 measure only the strength of the **M^{pro}**/inhibitor local repulsion-exchange and electrostatic
186 interactions. Because of the weight of dispersion in **M^{pro}**/inhibitor interactions, a $\Delta\bar{U}_{\text{inhi}}^{\text{pocket}}$
187 profile close to those of the four strong inhibitors **13a** to **11r** does not correspond necessarily
188 to a potent inhibitor, as for **11f**.

189 By employing a computational scheme which sequentially couples a multi-scale polariz-
190 able MM approach and a particularly efficient QM method, we have shown that the most
191 promising α -ketoamide inhibitors developed the Hilgenfeld’s team target mainly three pock-
192 ets of the **M^{pro}** catalytic domain, namely S1, S1’ and S2. Contrary to the recent large-scale
193 MD simulations study of Huynh et al,¹² both our PMFs (in particular those corresponding
194 to **11p** and **11f**) and fragmentation computations unambiguously show the inhibitor potency
195 not to be tied to the inhibitor capacity to strongly interact with the **M^{pro}** pocket S4 but
196 with pocket S2. Note that besides simulation artifacts underlined by Huynh et al (like the
197 accuracy of their scoring functions and of their standard pairwise force fields), the conclusion
198 of the latter authors may arise from their set of investigated drugs that were not able to
199 specifically target pocket S2.

200 Hence our computations strongly suggest **M^{pro}** pocket S2 to be a key anchoring site that
201 is able to lock within the **M^{pro}** catalytic domain an α -ketoamide inhibitor even before cova-
202 lently bonding to the **M^{pro}** catalytic cysteine occurs, which warrants the generality of that
203 conclusion. We may also note here that other promising **M^{pro}** inhibitors like the carmofur

204 one³ and the inhibitor N3² and related⁴ all target pocket S2 by means of hydrophobic groups
205 like cyclo-propyl or cyclo-hexyl, and even using a fluoro-phenyl group as shown by Dai et *al.*⁴
206 New inhibitors must target that pocket to provide thermodynamically stable **M^{pro}**/inhibitor
207 complexes, preferentially using the latter chemical groups.

208 **Supplementary Material Available**

209 This material is available free of charge via the Internet at <http://pubs.acs.org>. It pro-
210 vides more detailed discussions regarding the accuracy of the our multi scale MM ap-
211 proach to model proteins and α -ketoamide inhibitors in aqueous phase as well as of both
212 the MM and quantum PBE level of theory to describe these inhibitors in gas phase as
213 compared to high end quantum CCSD(T) computations. Discussions regarding the PBE
214 under-polarization of the enzyme covalent bonds are also presented and the details of the
215 **M^{pro}**/inhibitors structures, quantum and MM interaction energies and fragmentation data
216 (like the fragment assignment to **M^{pro}** pockets) are also provided. The final structures of the
217 **M^{pro}**/inhibitor complexes along all our MD simulations (in PDB format) are freely available
218 at <http://biodev.cea.fr/polaris/download.html>.

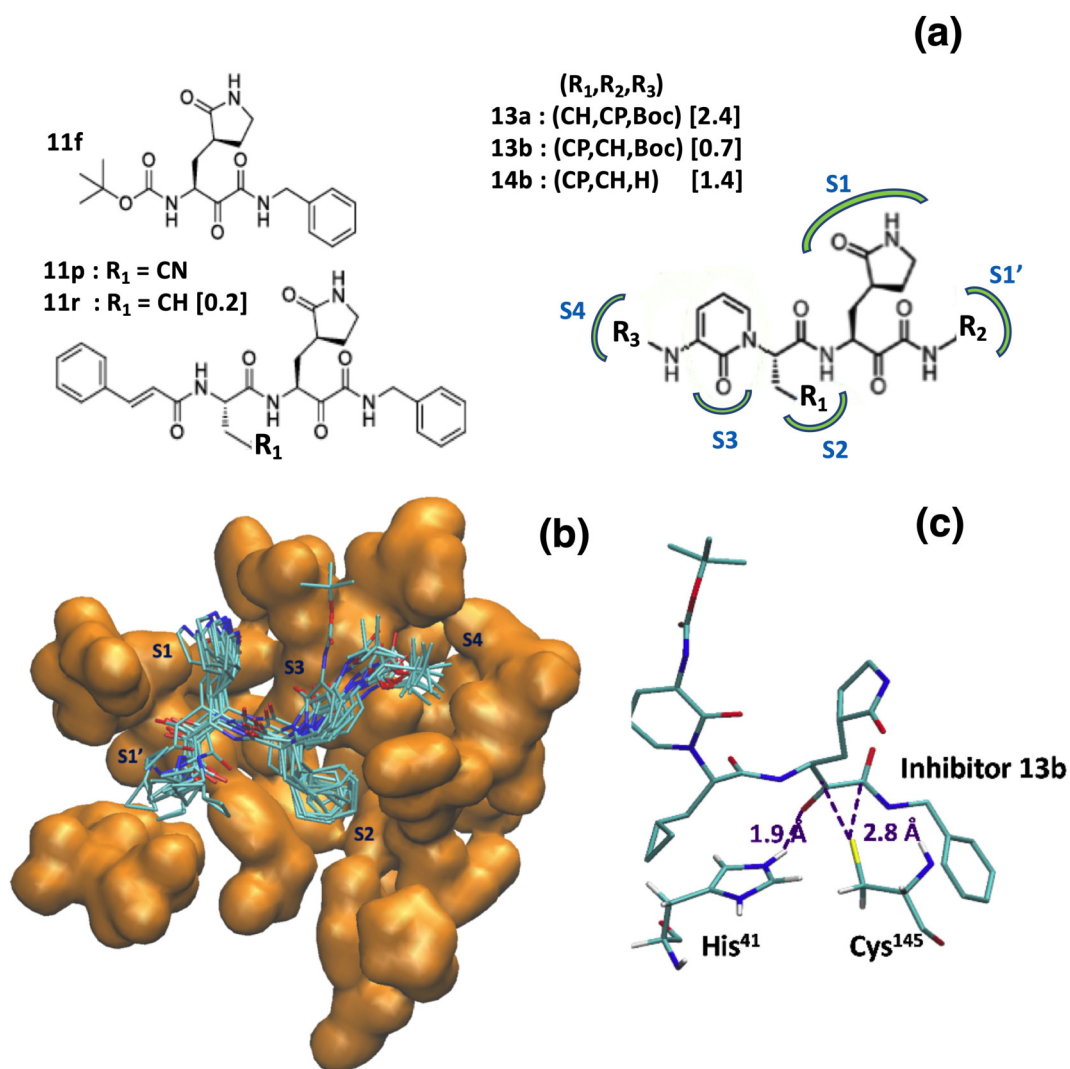


Figure 1: (a) Definition of the six α -ketoamide inhibitors considered in the present study. CN, CP, CH and Boc are the acetonitril, cyclo propyl, cyclo hexyl and tert-butyloxycarbonyl groups, respectively. In the brackets the EC_{50} values in μM unit that measure the inhibitor potency for the SARS-Cov-2 M^{Pro} main protease.¹ For inhibitors **13a**, **13b**, and **14b**, the interaction between their side chains and the M^{Pro} pockets S1 to S4 (as defined in Refs.^{4,17}) are shown. (b) Superimposition of the final inhibitor **13a** structures along the 10 independent MD simulations within the M^{Pro} catalytic binding site. (c) Detail of the M^{Pro} /inhibitor **13b** final structure along one of the simulations. Dashed lines are the strong hydrogen bond between the His⁴¹ imidazolium and the inhibitor ketoamide group and the Cys¹⁴⁵ sulfur/inhibitor ketoamide carbon sp^2 distances.

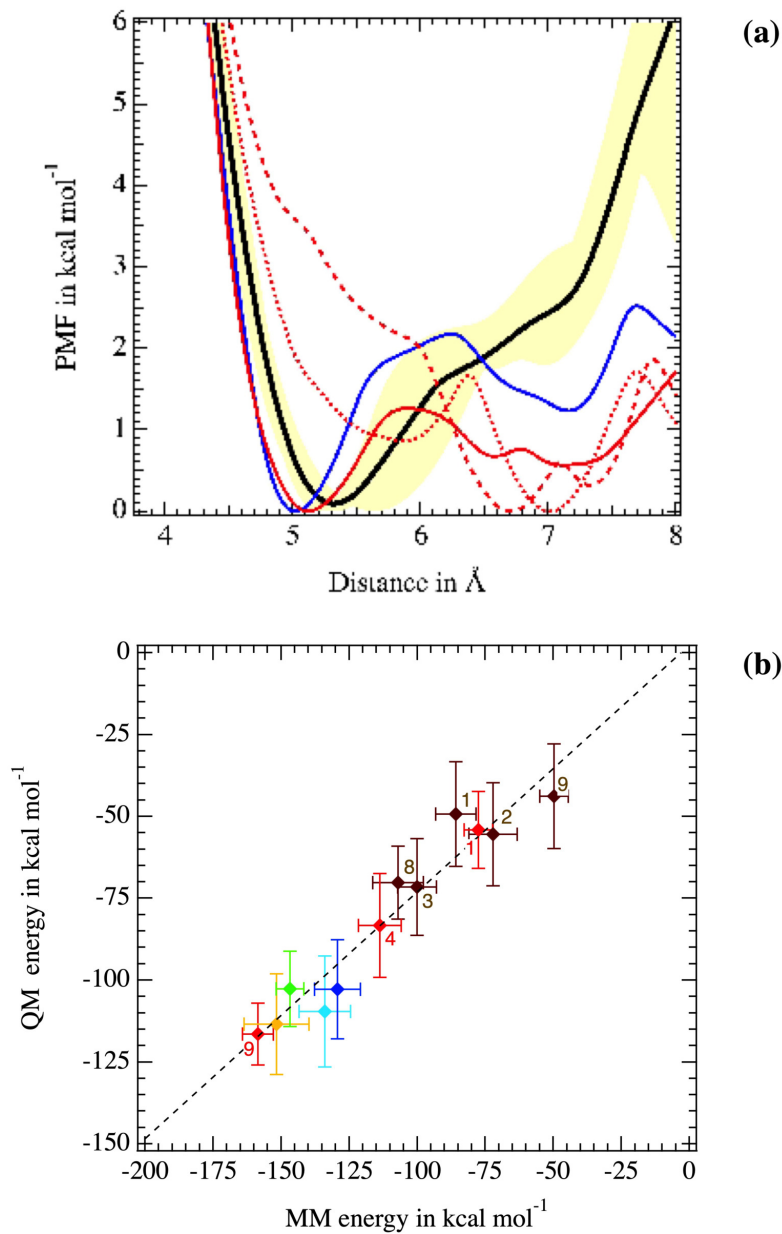


Figure 2: (a) Local PMF(r) profiles corresponding to the \mathbf{M}^{pro} /inhibitor complexes. Black line: mean PMF corresponding to inhibitors **11r**, **13a**, **13b** and **14b** (the yellow domain is defined by the minimum and maximum values of each single PMF). Blue: PMF of **11f**. Red: PMF^{**11p**}_{180°} (full line), PMF^{**11p**}_{-60°} (dashed line) and PMF^{**11p**}_{60°} (dotted line) corresponding to inhibitor **11p**, see text for definition. (b) Mean QM \mathbf{M}^{pro} /inhibitor interaction energies $\Delta\bar{U}$ as a function of their MM counter parts (brown **11f**, red **11fp**, orange **13a**, green **11r**, light blue **13b**, dark blue **14b**). The error bars correspond the standard deviations of these mean energy values. For **11f** and **11p** data, the numbers shown corresponds to the simulation labels (see Supporting Information).

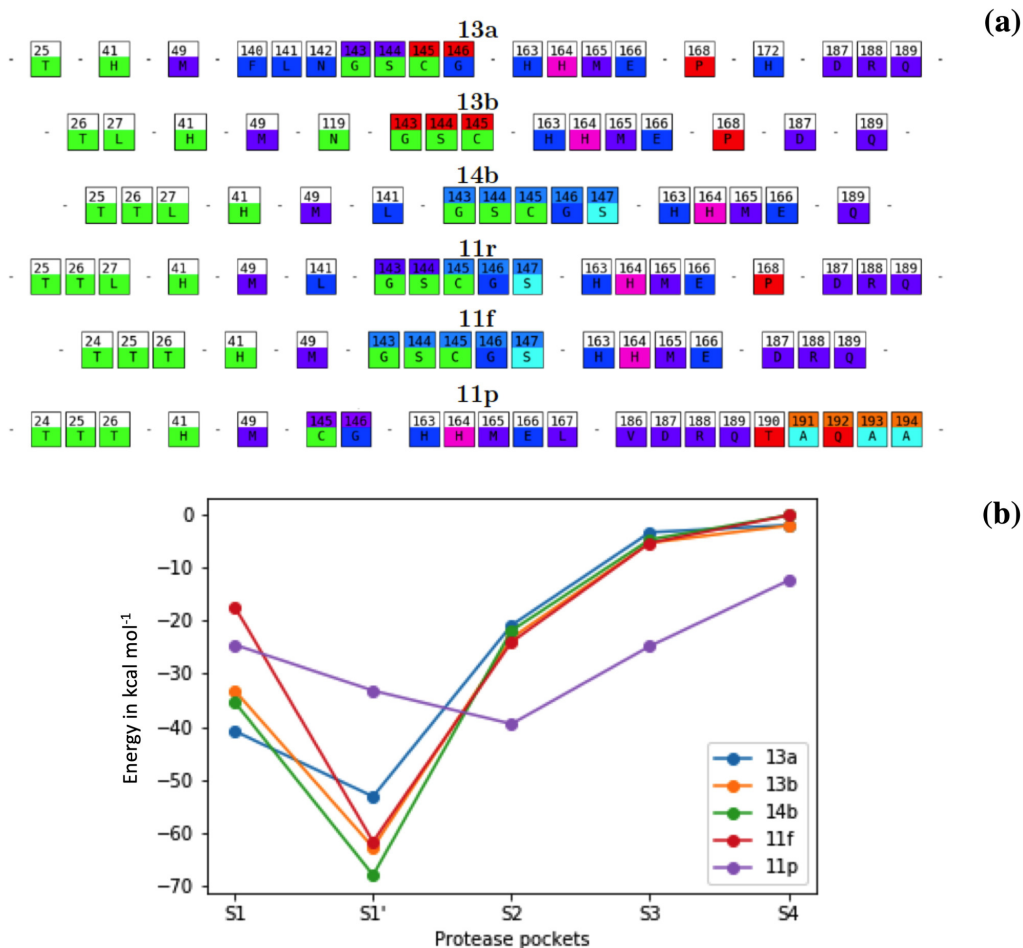


Figure 3: (a) \mathbf{M}^{pro} fragments interacting noticeably with the inhibitors (*i.e.* their corresponding fragment/inhibitor energy $\delta\bar{U}^{fi}$ is larger than $k_{\text{B}}T = 0.6 \text{ kcal mol}^{-1}$). Each box corresponds to a \mathbf{M}^{pro} residue, the box colors show, in the upper part, the regroupment in the QM fragments. Amino acids with similar colors belong to the same fragment. A white top color indicates that the amino acid itself constitutes a good fragment. The bottom colors indicate to which \mathbf{M}^{pro} catalytic pocket the corresponding amino-acid has been (arbitrarily) assigned. The pocket S1, S1', S2, S3 and S4 are colored, respectively, in (dark) blue, green, purple, pink and red. Because of the common residues delimiting the different pockets, we define pocket S3 from the single residue His¹⁶⁴. The cyan aminoacids have not been assigned to a pocket. (b) $\Delta\bar{U}_{\text{inhi}}^{\text{pocket}}$ inhibitor/protease pocket energies for the MD snapshot sets where the inhibitors maintain a standard interaction pattern. The corresponding standard deviations represent about 20 % of the strong mean $\Delta\bar{U}_{\text{inhi}}^{\text{pocket}}$ values up to 80 % of the weak ones. We can observe that the **11p** inhibitor has an outstanding pattern both on the fragmentation and on the pocket interactions. The strong $\Delta\bar{U}_{\text{inhi}}^{\text{S3}}$ value reported here for inhibitor **11p** arises from a hydrogen bond network between that inhibitor, the backbone CO and side chain imidazole group of His¹⁶⁴, and the amide side chain group of Gln¹⁸⁹ (see Supporting Information).

219 **Acknowledgments**

220 M.M. thanks Emmanuel Oseret (Exascale Computing Research Laboratory, a joint IN-
221 TEL/CEA/UVSQ/GENCI laboratory) for his help in optimizing the code POLARIS(MD).
222 This work was granted access to the TGCC HPC resources under the allocation 2019-2020
223 [A0070307078] and the Grand Challenge allocation [GC0429] made by GENCI. L.G. and
224 W.D. also gratefully acknowledge the joint CEA-RIKEN collaboration action. We also ac-
225 knowledge support from the MaX EU Center of Excellence. We are also grateful to the fi-
226 nancial support by the Labex CaPPA (contract ANR-11-LABX-0005-01) and I-SITE ULNE
227 project OVERSEE (contract ANR-16-IDEX-0004), and by the CPER CLIMIBIO (European
228 Regional Development Fund, Hauts de France council, French Ministry of Higher Education
229 and Research).

References

- (1) Zhang, L.; Lin, D.; Sun, X.; Curth, U.; Drosten, C.; Sauerhering, L.; Becker, S.; Rox, K.; Hilgenfeld, R. Crystal Structure of SARS-CoV-2 Main Protease Provides a Basis for Design of Improved α -Ketoamide Inhibitors. *Science* **2020**, *368*, 409–412, DOI: 10.1126/science.abb3405.
- (2) Jin, Z.; Du, X.; Xu, Y.; Deng, Y.; Liu, M.; Zhao, Y.; Zhang, B.; Li, X.; Zhang, L.; Peng, C. et al. Structure of Mpro from SARS-CoV-2 and Discovery of its Inhibitors. *Nature* **2020**, *582*, 289–293, DOI: 10.1038/s41586-020-2223-y.
- (3) Jin, Z.; Zhao, Y.; Sun, Y.; Zhang, B.; Wang, H.; Wu, Y.; Zhu, Y.; Zhu, C.; Hu, T.; Du, X. et al. Structural Basis for the Inhibition of SARS-CoV-2 Main Protease by Antineoplastic Drug Carmofur. *Nat. Struct. Mol. Biol.* **2020**, *27*, 529–532, DOI: 10.1038/s41594-020-0440-6.
- (4) Dai, W.; Zhang, B.; Jiang, X.-M.; Su, H.; Li, J.; Zhao, Y.; Xie, X.; Jin, Z.; Peng, J.; Liu, F. et al. Structure-Based Design of Antiviral Drug Candidates Targeting the SARS-CoV-2 Main Protease. *Science* **2020**, *368*, 1331–1335, DOI: 10.1126/science.abb4489.
- (5) VanPatten, S.; He, M.; Altit, A.; F Cheng, K.; Ghanem, M. H.; Al-Abed, Y. Evidence Supporting the Use of Peptides and Peptidomimetics as Potential SARS-CoV-2 (COVID-19) Therapeutics. *Future Med. Chem.* **0**, *0*, null, DOI: 10.4155/fmc-2020-0180.
- (6) Ratcliff, L. E.; Dawson, W.; Fisicaro, G.; Caliste, D.; Mohr, S.; Degomme, A.; Videau, B.; Cristiglio, V.; Stella, M.; D 'Alessandro, M. et al. Flexibilities of Wavelets as a Computational Basis Set for Large-Scale Electronic Structure Calculations. *J. Chem. Phys.* **2020**, *152*, 194110, DOI: 10.1063/5.0004792.

- 254 (7) Genovese, L.; Neelov, A.; Goedecker, S.; Deutsch, T.; Ghasemi, S. A.; Willand, A.;
255 Caliste, D.; Zilberberg, O.; Rayson, M.; Bergman, A. et al. Daubechies Wavelets as a
256 Basis Set for Density Functional Pseudopotential Calculations. *J. Chem. Phys.* **2008**,
257 *129*, 014109, DOI: 10.1063/1.2949547.
- 258 (8) Dawson, W.; Mohr, S.; Ratcliff, L. E.; Nakajima, T.; Genovese, L. Complexity Reduc-
259 tion in Density Functional Theory Calculations of Large Systems: System Partition-
260 ing and Fragment Embedding. *J. Chem. Theory Comput.* **2020**, *16*, 2952–2964, DOI:
261 10.1021/acs.jctc.9b01152.
- 262 (9) Mohr, S.; Masella, M.; Ratcliff, L. E.; Genovese, L. Complexity Reduction in Large
263 Quantum Systems: Fragment Identification and Population Analysis via a Local
264 Optimized Minimal Basis. *J. Chem. Theory Comput.* **2017**, *13*, 4079–4088, DOI:
265 10.1021/acs.jctc.7b00291.
- 266 (10) Masella, M.; Borgis, D.; Cuniasse, P. Combining a Polarizable Force-Field and a Coarse-
267 Grained Polarizable Solvent Model: Application to Long Dynamics Simulations of
268 Bovine Pancreatic Trypsin Inhibitor. *J. Comput. Chem.* **2008**, *29*, 1707–1724, DOI:
269 10.1002/jcc.20932.
- 270 (11) Masella, M.; Borgis, D.; Cuniasse, P. Combining a Polarizable Force-Field and a Coarse-
271 Grained Polarizable Solvent Model. II. Accounting for Hydrophobic Effects. *J. Comput.*
272 *Chem.* **2011**, *32*, 2664–2678, DOI: 10.1002/jcc.21846.
- 273 (12) Huynh, T.; Wang, H.; Luan, B. In Silico Exploration of the Molecular Mechanism
274 of Clinically Oriented Drugs for Possibly Inhibiting SARS-CoV-2’s Main Protease. *J.*
275 *Phys. Chem. Lett.* **2020**, *11*, 4413–4420, DOI: 10.1021/acs.jpcllett.0c00994.
- 276 (13) Khan, S. A.; Zia, K.; Ashraf, S.; Uddin, R.; Ul-Haq, Z. Identification of Chymotrypsin-
277 Like Protease Inhibitors of SARS-CoV-2 via Integrated Computational Approach. *J.*
278 *Biomol. Struct. Dyn.* **2020**, *0*, 1–10, DOI: 10.1080/07391102.2020.1751298.

- 279 (14) Gentile, D.; Patamia, V.; Scala, A.; Sciortino, M.; Piperno, A.; Rescifina, A. Putative
280 Inhibitors of SARS-CoV-2 Main Protease from A Library of Marine Natural Products:
281 A Virtual Screening and Molecular Modeling Study. *Mar. Drugs* **2020**, *18*, 225, DOI:
282 10.3390/md18040225.
- 283 (15) Kumar, S.; Sharma, P. P.; Shankar, U.; Kumar, D.; Joshi, S. K.; Pena, L.; Durva-
284 sula, R.; Kumar, A.; Kempaiah, P.; Poonam, et al. Discovery of New Hydroxyethy-
285 lamine Analogs against 3CLpro Protein Target of SARS-CoV-2: Molecular Docking,
286 Molecular Dynamics Simulation, and Structure-Activity Relationship Studies. *J. Chem.*
287 *Inf. Model.* **0**, *0*, null, DOI: 10.1021/acs.jcim.0c00326.
- 288 (16) Hatada, R.; Okuwaki, K.; Mochizuki, Y.; Handa, Y.; Fukuzawa, K.; Komeiji, Y.;
289 Okiyama, Y.; Tanaka, S. Fragment Molecular Orbital Based Interaction Analyses on
290 COVID-19 Main Protease - Inhibitor N3 Complex (PDB ID: 6LU7). *J. Chem. Inf.*
291 *Model.* **2020**, *60*, 3593–3602, DOI: 10.1021/acs.jcim.0c00283.
- 292 (17) Zhang, L.; Lin, D.; Kusov, Y.; Nian, Y.; Ma, Q.; Wang, J.; von Brunn, A.; Leysen, P.;
293 Lanko, K.; Neyts, J. et al. α -Ketoamides as Broad-Spectrum Inhibitors of Coronavirus
294 and Enterovirus Replication: Structure-Based Design, Synthesis, and Activity Assess-
295 ment. *J. Med. Chem.* **2020**, *63*, 4562–4578, DOI: 10.1021/acs.jmedchem.9b01828.
- 296 (18) Tichá, A.; Stanchev, S.; Vinothkumar, K. R.; Mikles, D. C.; Pachel, P.; Be-
297 gan, J.; Škerle, J.; Švehlova, K.; Nguyen, M.; Verhelst, S. et al. General and Mod-
298 ular Strategy for Designing Potent, Selective, and Pharmacologically Compliant In-
299 hibitors of Rhomboid Proteases. *Cell Chem. Biol.* **2017**, *24*, 1523 – 1536.e4, DOI:
300 10.1016/j.chembiol.2017.09.007.
- 301 (19) Świderek, K.; Moliner, V. Revealing the Molecular Mechanisms of Proteolysis of
302 SARS-CoV-2 Mpro by QM/MM Computational Methods. *Chem. Sci.* **2020**, –, DOI:
303 10.1039/D0SC02823A, Advance Article.

- 304 (20) Pillaiyar, T.; Manickam, M.; Namasivayam, V.; Hayashi, Y.; Jung, S.-H. An Overview
305 of Severe Acute Respiratory Syndrome–Coronavirus (SARS-CoV) 3CL Protease In-
306 hibitors: Peptidomimetics and Small Molecule Chemotherapy. *J. Med. Chem.* **2016**,
307 *59*, 6595–6628, DOI: 10.1021/acs.jmedchem.5b01461.
- 308 (21) Zhang, L.; Lin, D.; Hilgenfeld, R. Crystal structure of the complex resulting
309 from the reaction between the SARS-CoV main protease and tert-butyl (1-
310 ((S)-3-cyclohexyl-1-(((S)-4-(cyclopropylamino)-3,4-dioxo-1-((S)-2-oxopyrrolidin-3-
311 yl)butan-2-yl)amino)-1-oxopropan-2-yl)-2-oxo-1,2-dihydropyridin-3-yl)carbamate.
312 DOI: 10.2210/pdb6Y7M/pdb.
- 313 (22) Kovalevsky, A.; Kneller, D.; Coates, L. Joint neutron/X-ray structure of SARS-CoV-2
314 3CL Mpro at room temperature. DOI:10.2210/pdb7JUN/pdb.
- 315 (23) <http://biodev.cea.fr/polaris/>.
- 316 (24) Anand, K.; Palm, G. J.; Mesters, J. R.; Siddell, S. G.; Ziebuhr, J.; Hilgen-
317 feld, R. Structure of Coronavirus Main Proteinase Reveals Combination of a Chy-
318 motrypsin Fold with an extra α -Helical Domain. *EMBO J.* **2002**, *21*, 3213–3224,
319 DOI: 10.1093/emboj/cdf327.
- 320 (25) Masella, M.; Cuniasse, P. A Many-Body Model to Study Proteins. I. Applications to
321 MLn^{m+} Complexes, $M^{m+} = Li^+, Na^+, K^+, Mg^{2+}, Ca^{2+}$, and Zn^{2+} , $L = H_2O, CH_3OH,$
322 $HCONH_2$, $n = 1-6$, and to Small Hydrogen Bonded Systems. *J. Chem. Phys.* **2003**, *119*,
323 1866–1873, DOI: 10.1063/1.1579478.
- 324 (26) Houriez, C.; Meot-Ner (Mautner), M.; Masella, M. Solvation of the Guanidinium
325 Ion in Pure Aqueous Environments: A Theoretical Study from an Ab Initio-
326 Based Polarizable Force Field. *J. Phys. Chem. B* **2017**, *121*, 11219–11228, DOI:
327 10.1021/acs.jpcc.7b07874.

- 328 (27) Schröder, H.; Creon, A.; Schwabe, T. Reformulation of the D3(Becke-Johnson) Disper-
329 sion Correction without Resorting to Higher than C6 Dispersion Coefficients. *J. Chem.*
330 *Theory Comput.* **2015**, *11*, 3163–3170, DOI: 10.1021/acs.jctc.5b00400.
- 331 (28) You, W.; Tang, Z.; Chang, C.-e. A. Potential Mean Force from Umbrella Sampling
332 Simulations: What Can We Learn and What Is Missed? *J. Chem. Theory Comput.*
333 **2019**, *15*, 2433–2443, DOI: 10.1021/acs.jctc.8b01142.
- 334 (29) Ratcliff, L. E.; Mohr, S.; Huhs, G.; Deutsch, T.; Masella, M.; Genovese, L. Challenges
335 in Large Scale Quantum Mechanical Calculations. *WIREs Computational Molecular*
336 *Science* **2017**, *7*, e1290, DOI: 10.1002/wcms.1290.